Geothermics 74 (2018) 181–189

Contents lists available at ScienceDirect

Geothermics

journal homepage: www.elsevier.com/locate/geothermics

Assessing the role of fractures on the permeability of the Permo-Triassic sandstones at the Soultz-sous-Forêts (France) geothermal site

Alexandra R.L. Kushnir*, Michael J. Heap, Patrick Baud

Géophysique Expérimentale, Institut de Physique du Globe de Strasbourg (UMR 7516, CNRS, Université de Strasbourg/EOST), 5 rue René Descartes, 67084, Strasbourg Cedex, France

ARTICLE INFO

Keywords:
Buntsandstein
Upper Rhine Graben
Reservoir permeability
Upscaling
Hydraulic conductivity
EPS-1

ABSTRACT

Quantification of the systemic permeability of geothermal reservoirs is essential to the assessment of their economic feasibility. Here we investigate experimentally the role of fractures on the permeability of a 400 m-thick unit of Permo-Triassic sandstone from the EPS-1 exploration borehole in the Upper Rhine Graben near Soultz-sous-Forêts (France). The permeability of initially intact sandstone samples was measured before and after the introduction of a through-going tensile fracture. While the permeability of the fracture-free samples varied over five orders of magnitude between 1×10^{-19} and 1×10^{-14} m^2, the presence of through-going fractures increased sample permeability to between 8×10^{-14} and 4×10^{-12} m^2. Using the fracture aperture of open fractures provided by borehole televiewer data, we model the equivalent permeability down the borehole to be between 7×10^{-18} and 3×10^{-13} m^2, which is in agreement with values of hydraulic conductivity determined using borehole tests. Overall, these equivalent permeability values are not sufficiently high to sustain hydrothermal convection at Soultz-sous-Forêts, highlighting the need for continued anthropogenic stimulation.

1. Introduction

The economic viability of Enhanced Geothermal Systems (EGS) relies on the continuous movement of hydrothermal fluids within an active reservoir. For example, the development of economically feasible reservoirs in the Upper Rhine Graben (e.g. Soultz-sous-Forêts, France; Fig. 1) requires the presence of sustained kilometre-scale hydrothermal convection cells between the crystalline reservoir rock and the overlying sedimentary sequences. The convection of hot fluids in these systems can only be maintained above a threshold reservoir permeability (Pribnow and Schellschmidt, 2000; Lundgren et al., 2004; Graf and Therrien, 2009; Guillou-Frottier et al., 2013; Magnenet et al., 2014) and requires the presence of a network of open, reservoir-scale fractures (Genter et al., 1997; Haffen et al., 2013; Vidal et al., 2015).

In general, fluid circulation within the crust is reliant on large fracture networks (Walsh, 1981; Caine et al., 1996; Min et al., 2004). However, laboratory measurements have shown that the presence of shear fractures may act to both increase and decrease permeability in rock. While shear fractures in porous sandstones ($0.15 < \phi < 0.35$) may reduce rock permeability (Zhu and Wong, 1997), increases in permeability are observed with increasing inelastic strain in low porosity granite (Brace, 1978; Mitchell and Faulkner, 2008) and volcanic rock (Farquharson et al., 2016a). Similarly, laboratory studies have shown that extension fractures can increase the permeability of rock by several orders of magnitude (Morrow et al., 2001; Nara et al., 2011; Heap and Kennedy, 2016; Hofmann et al., 2016; Wang et al., 2016; Lamur et al., 2017; Pérez-Flores et al., 2017). The morphology of extension fractures plays a key role in governing fracture permeability, whereby increased fracture tortuosity (Heap and Kennedy, 2016) and roughness (Brown, 1987; Thompson and Brown, 1991; Zimmerman et al., 1992) act to decrease permeability. Further, the presence of fracture filling materials reduces permeability to varying degrees (Pérez-Flores et al., 2017). For instance, while fracture permeability is reduced by the presence of fault gouge, this decrease is moderated by particle size, where finer particle sizes act to more efficiently curtail fluid flow (Wang et al., 2016). Mineral precipitation also acts to effectively seal fractures and reduce permeability (Summers et al., 1978; Moore et al., 1994; Morrow et al., 2001), which can be especially disruptive to geothermal energy exploitation (Christy and Putnis, 1993; Scheiber et al., 2013).

The influence of open fracture space on rock permeability is often assessed using the cubic law (Witherspoon et al., 1980; Tsang, 1984; Pyrak-Nolte et al., 1987; Zimmerman and Bodvarsson, 1996), which models the permeability of a fracture as $k_f = \frac{d^2}{12}$, where d is the fracture aperture. The cubic law models laminar fluid flow between smooth parallel plates and is appropriately used when fracture apertures are

* Corresponding author.
E-mail addresses: alexandra.kushnir@gmail.com, akushnir@unistra.fr (A.R.L. Kushnir).

https://doi.org/10.1016/j.geothermics.2018.03.009
Received 12 September 2017; Received in revised form 1 March 2018; Accepted 13 March 2018

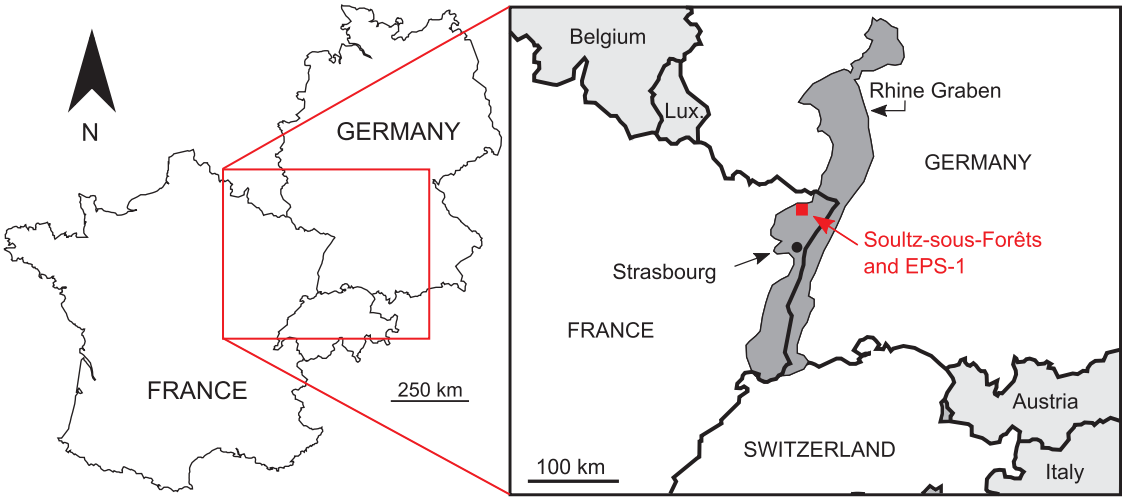

Fig. 1. Map of the Rhine Graben showing the location the EPS-1 exploratory borehole, approximately 5 km away from Soultz-sous-Forêts (France).

large or when fracture surfaces are smooth and straight. Under certain circumstances, however, rock fractures are not adequately described by ideal parallel plates (Brown, 1987; Pyrak-Nolte et al., 1987; Brown, 1989); as fracture tortuosity and fracture roughness increase, for instance, the fracture surfaces may be brought together and flow rates can deviate from those predicted using the cubic law (Tsang, 1984; Brown, 1987; Pyrak-Nolte et al., 1987; Zimmerman et al., 1992; Zimmerman and Bodvarsson, 1996). Indeed, when fractures are rough-walled, determining fracture aperture often becomes non-trivial (Witherspoon et al., 1980; Pyrak-Nolte et al., 1987; Brown, 1989; Zimmerman and Bodvarsson, 1996). Under these conditions, predicted permeability values may be significantly larger than those measured in the laboratory, though as much as 30% of the fracture surface may need to be in contact for laboratory measurements to deviate appreciably from models (Tsang, 1984).

Alternatively, the role of fractures on rock permeability can be investigated by adopting an effective medium approach (Vajdova et al., 2004; Baud et al., 2012; Heap and Kennedy, 2016; Hofmann et al., 2016; Farquharson et al., 2017a). This method assumes that the equivalent transmissivity of a unit of rock containing a planar structural feature oriented parallel to the direction of fluid flow can be described by:

$$Ak = A_i k_i + A_f k_f \quad (1)$$

where A is the cross-sectional area of the entire rock unit perpendicular to flow, k is the equivalent permeability of the rock unit, A_i is the cross-sectional area of the intact rock, k_i is the permeability of the intact rock, A_f is the cross-sectional area of the structural feature, and k_f is the permeability of the structural feature (Fig. 2A). Importantly, this effective medium approach considers the contribution of the proportions of both the structural feature and the intact rock to overall permeability. This method is especially convenient in the case of fractured rocks when the permeability of the intact and fractured rock can be measured in the laboratory since it avoids the necessity of characterizing fracture topography and is mathematically less sensitive to fracture aperture than the cubic law.

The Upper Rhine Graben is characterized by a crystalline (Paleozoic granite) basement (Genter and Traineau, 1996) overlain by Permo-Triassic sediments (Aichholzer et al., 2016). The geothermal potential within the Upper Rhine Graben is constrained to an extensive zone of geothermal convection between 1 and 3.5 km depth, where the geothermal gradient is 5 °C/km (Pribnow and Schellschmidt, 2000); the top of this convection zone is rooted in the Permo-Triassic sandstones and overlying Triassic Muschelkalk sediments (Vidal et al., 2015). Tertiary and Mesozoic sediments overlie the convective zone, acting as a regionally low-permeable layer that caps and insulates the hydrothermal system (Pribnow and Schellschmidt, 2000; Vidal et al., 2015). While the Paleozoic granite basement is currently being exploited as the reservoir at the Soultz-sous-Forêts (Kappelmeyer et al., 1991; Baria et al., 1999; Gérard et al., 2006) and Rittershoffen (France) (Baujard et al., 2017) EGS sites, the transition between the granite and overlying sediments is also of economic interest. Indeed, the geothermal potential of this transition zone has been demonstrated at Cronenbourg and Rittershoffen (France) and Landau, Insheim, and Bruchsal (Germany) (Housse, 1984; Baumgärtner and Lerch, 2013; Hettkamp et al., 2013; Villadangos, 2013).

Most geothermal-related research in the Rhine Graben has focused on the crystalline basement (Genter and Traineau, 1996; Genter et al., 1997; Sausse et al., 2006; Dezayes et al., 2010; Ledesert et al., 2010), while relatively few studies have looked at the role of permeability within the sedimentary cover (Haffen et al., 2013; Vidal et al., 2015; Griffiths et al., 2016; Heap et al., 2017). The matrix permeability of the Permo-Triassic sedimentary cover, including the Buntsandstein, varies over five orders of magnitude (between 10^{-19} and 10^{-13} m^2) (Griffiths et al., 2016; Heap et al., 2017). While these studies have shown that there is no appreciable permeability anisotropy in most of the Buntsandstein, some units are more permeable parallel to bedding − rather than perpendicular to bedding – by less than an order of magnitude. Critically, the permeability of the matrix of most of the Buntsandstein units is below the numerically modelled threshold permeability required to sustain kilometre-scale convection cells in the Soultz-sous-Forêts geothermal system (Graf and Therrien, 2009; Magnenet et al., 2014). Regional hydrothermal convection is sustained, instead, by a series of fracture zones that regionally increase the permeability of the sedimentary cover (Vidal et al., 2015). However, these fractures can be subject to rapid sealing due to secondary mineral precipitation (Griffiths et al., 2016), requiring periodic anthropogenic stimulation of the reservoir to reopen permeable pathways.

Assessing the role of reservoir-scale structural features on the hydraulic properties of reservoirs is challenging. Physical property measurements made in the laboratory are limited by sample size thus, while the physical properties of intact rock are easily characterized, such measurements preclude the effect of larger-scale structural features, such as fracture networks. Indeed, comparing permeability data from intact core samples (Griffiths et al., 2016; Heap et al., 2017), which represent the matrix permeability of the reservoir rock, with the hydraulic conductivity determined from large-scale borehole hydraulic tests demonstrates that the matrix permeability is often far lower than that of the reservoir as a whole (Stober and Bucher, 2015). In this study, we investigate experimentally - using the effective medium approach -

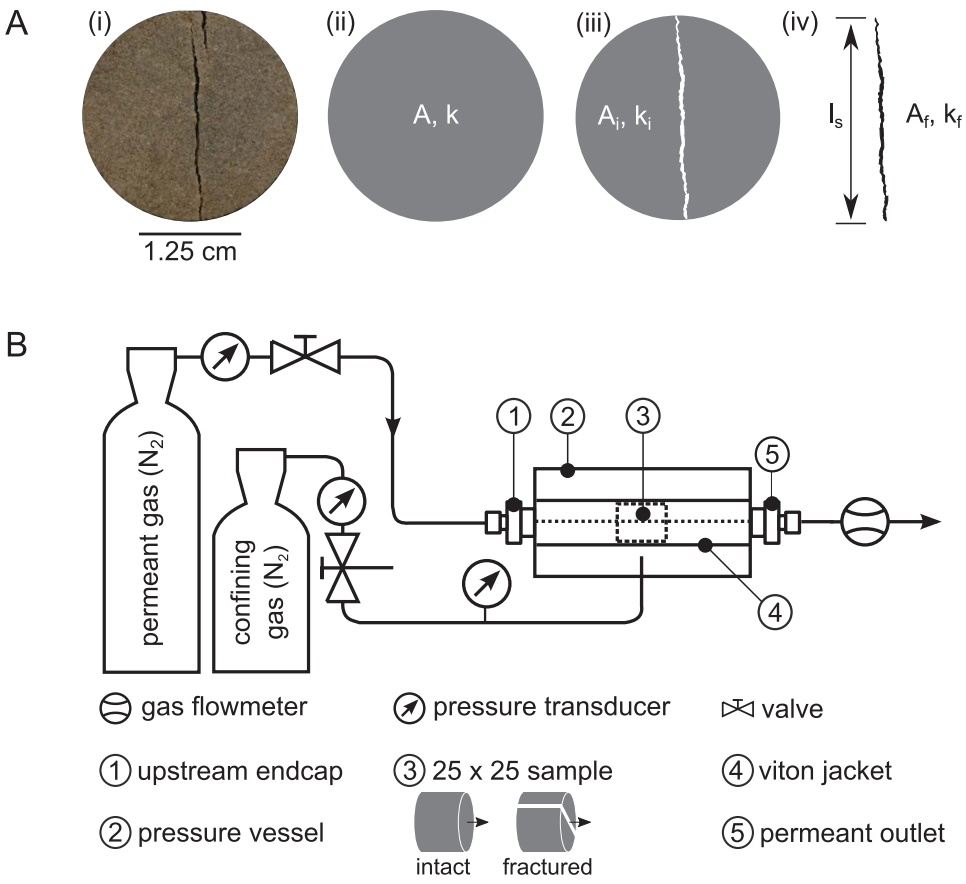

Fig. 2. A. Dimensions and permeability values used to determine fracture permeability using the effective medium approach (see Eq. (1)). The schematic presents the surface expression of a fracture on the end-face of a cylindrical sample investigated in the present study. (i) Photograph of the end-face of a fractured sample. (ii) A is the cross-sectional area and k is the permeability of the fractured sample. (iii) A_i is the cross-sectional area and k_i is the permeability of the intact part of the sample. (iv) A_f is the cross-sectional area of the fracture and k_f is the permeability of the fracture. l_s is the shortest length between the tips of the fracture. B. Schematic of the nitrogen gas permeameter used in the present study, modified from Farquharson et al. (2016b) and Heap and Kennedy (2016). Schematics of the cylindrical samples before and after the introduction of a through-going tensile fracture are shown. Fluid flow is parallel to the cylinder axis during permeability measurements, as indicated by the black arrows.

the role of fractures on the permeability of a 400 m-thick unit of Permo-Triassic sandstone sampled from the EPS-1 exploration borehole near Soultz-sous-Forêts. We determine the influence of experimentally created tensile fractures on the permeability of samples of initially intact sandstones. We then use these data in conjunction with borehole televiewer data to inform modelling of the metre-scale rock permeability down the EPS-1 borehole.

2. Experimental materials

We have selected sandstones drilled at the EPS-1 exploratory geothermal well located near Soultz-sous-Forêts (Fig. 1). Samples of intact rock (i.e. free of fractures on the borehole scale) were collected at roughly 50 m intervals along the 400 m length of the Permo-Triassic sediments, between 1006 and 1417 m borehole depth. These rocks span the entire Buntsandstein stratigraphy and include the Permian *Annweiler* and *Anté-Annweiler* horizons that directly overly the Paleozoic granite basement (Aichholzer et al., 2016). In total, sandstones from 12 different horizons were sampled: one from the *Voltzia* unit, one from the *Couches Intermédiaires* unit, three from the *Karlstal* unit, two from the *Rehberg* unit, two from the *Trifels* unit, two from the *Annweiler* unit, and one from the *Anté-Annweiler* unit (see Aichholzer et al. (2016) for a complete stratigraphic column). These rocks have connected porosities between 0.03 and 0.19 and negligible isolated porosity (Griffiths et al., 2016; Heap et al., 2017). The average grain sizes of the sandstones is between 142 and 424 μm (Heap et al. (2017); Table 1). The sandstones are hydrothermally altered, manifest as pore-filling clays (illite-smectite, between 2 and 13 wt.%; Table 1), dolomite, siderite, barite, and altered feldspars. For a detailed description of the mineralogy and microstructure of the rocks used in this study see Heap et al. (2017).

3. Experimental methods

Two cylindrical samples (25 mm in diameter) were cored from each of the twelve borehole samples collected and precision-ground to a nominal length of 25 mm to ensure a length to diameter ratio of unity. Each sample was cored parallel to the plunge of the EPS-1 borehole (approximately perpendicular to bedding), washed, and dried under vacuum at 40 °C for at least 48 h. The connected porosities of the dried samples were determined using helium pycnometry (Micromeritrics AccuPyc II 1340) (Table 1).

In this study we measured the permeability of each sample i) before deformation (hereafter referred to as the permeability of the intact material, k_i) and ii) after deformation (hereafter referred to as the permeability of the fractured sample, k).

3.1. Permeability measurements

The permeability of each sample was measured using a benchtop nitrogen gas permeameter (Fig. 2B; Farquharson et al. (2016b)) using a steady-state flow (for high permeability) or transient pulse (for low permeability) configuration under a confining pressure of 1 MPa and at ambient laboratory temperature (Heap et al., 2017).

For samples with relatively high permeability (i.e. $k > 10^{-17}$ m^2), we measured permeability using the steady-state flow method. Using this method, the volumetric flow rate, Q, was measured using a gas flowmeter at several pressure gradients, ΔP (defined here as the upstream pressure, P_u, minus the downstream pressure, P_d). In our system, P_d is atmospheric pressure and values of ΔP were typically between 0.005–0.2 MPa. Permeability, k_D, was then calculated using Darcy's Law for a compressible fluid:

$$k_D = \frac{Q}{P_m(P_u - P_d)} \frac{\mu L P_d}{A}, \quad (2)$$

Table 1
Porosity and permeability data. Clay content is the muscovite/illtie-smectite content for each sample; ϕ_c – connected gas porosity; k_i – permeability of the intact sample; k – permeability of the fractured sample. τ – fracture tortuosity, determined by image analysis; d – fracture width, determined by image analysis; k_f – calculated fracture permeability. Clay content and average grain size from Heap et al. (2017). '-' denotes samples which contained more than one through-going fracture; these samples were not included in the study.

sample	layer	depth [m]	average grain size [μm]	clay content [wt.%]	ϕ_c	k_i[m^2]	k [m^2]	τ	d [mm]	k_f[m^2]
84_1	Voltzia	1008	142	6	0.11	1.61×10^{-17}	1.24×10^{-13}	1.03	0.18	1.44×10^{-11}
84_2	Voltzia	1008	142	6	0.10	2.28×10^{-17}	3.10×10^{-12}	1.09	0.79	1.67×10^{-10}
100_1	Intermédiaires	1022	306	5	0.06	3.79×10^{-18}	8.20×10^{-14}	1.07	0.22	1.47×10^{-11}
100_2	Intermédiaires	1022	306	5	0.07	6.94×10^{-18}	–	–	–	–
157_1	Karlstal	1069	424	2	0.11	1.76×10^{-16}	7.58×10^{-13}	1.06	0.35	9.28×10^{-11}
157_2	Karlstal	1069	424	2	0.11	1.55×10^{-16}	8.13×10^{-13}	1.07	0.36	9.64×10^{-11}
198_1	Karlstal	1107	192	3.2	0.09	1.92×10^{-16}	3.30×10^{-13}	1.05	0.38	3.65×10^{-11}
198_2	Karlstal	1107	192	3.2	0.09	3.65×10^{-16}	2.70×10^{-12}	1.06	0.55	1.98×10^{-10}
248_1	Karlstal	1151	294	2.8	0.14	4.78×10^{-15}	1.62×10^{-12}	1.09	0.41	1.75×10^{-10}
248_2	Karlstal	1151	294	2.8	0.14	5.83×10^{-15}	1.19×10^{-12}	1.06	0.39	1.21×10^{-10}
299_1	Rehberg	1197	332	7.3	0.13	7.23×10^{-18}	–	–	–	–
299_2	Rehberg	1197	332	7.3	0.13	1.67×10^{-17}	1.50×10^{-12}	1.02	0.36	2.11×10^{-10}
347_1	Rehberg	1239	367	3.8	0.18	8.38×10^{-15}	3.80×10^{-13}	1.11	0.31	7.82×10^{-11}
347_2	Rehberg	1239	367	3.8	0.19	9.80×10^{-15}	2.83×10^{-13}	1.08	0.35	3.15×10^{-11}
402_1	Trifels	1290	259	3.5	0.13	3.29×10^{-16}	1.60×10^{-12}	1.04	0.56	1.18×10^{-10}
402_2	Trifels	1290	259	3.5	0.13	3.18×10^{-16}	7.49×10^{-13}	1.05	0.38	8.66×10^{-11}
453_1	Trifels	1336	361	3	0.17	4.12×10^{-15}	1.33×10^{-12}	1.08	0.38	1.42×10^{-10}
453_2	Trifels	1336	361	3	0.18	8.20×10^{-15}	3.68×10^{-13}	1.07	0.30	4.73×10^{-11}
497_1	Annweiler	1376	291	7.8	0.03	1.07×10^{-18}	4.39×10^{-13}	1.03	0.26	7.39×10^{-11}
497_2	Annweiler	1376	291	7.8	0.03	1.53×10^{-18}	–	–	–	–
508_1	Annweiler	1386	199	8.3	0.07	5.26×10^{-19}	1.60×10^{-12}	1.04	0.46	1.48×10^{-10}
508_2	Annweiler	1386	199	8.3	0.08	4.23×10^{-19}	–	–	–	–
540_1	Anté-Annweiler	1414	379	13.1	0.08	1.97×10^{-17}	–	–	–	–
540_2	Anté-Annweiler	1414	379	13.1	0.08	3.79×10^{-17}	1.37×10^{-12}	1.05	0.50	1.15×10^{-10}

where Q is the volumetric flow rate measured downstream of the sample, P_m is the mean pore fluid pressure (i.e., $(P_u + P_d)/2$), μ is the viscosity of the pore fluid (taken as the viscosity of nitrogen at 20 °C = 1.76×10^{-5} Pa.s), and L and A are the sample length and cross sectional area, respectively. If fluid flow is laminar, then Q and $P_m(P_u - P_d)$ are linearly related and k_D is calculated using the slope of the line of best fit of this linear relationship. While a linear relationship attests that the data are well described by Darcy's Law, the data should still be assessed for the Forchheimer (Forchheimer, 1901) and Klinkenberg (Klinkenberg, 1941) effects, described below.

When the permeability of a sample was too low to be measured using the steady-state flow method (i.e. k < 10^{-17} m^2), we employed the transient pulse method (Brace et al., 1968) modified for a downstream pore fluid reservoir of infinite volume and at atmospheric pressure. A full derivation of the equations presented below can be found in Heap et al. (2017). Using this method, k_D is determined by monitoring the decay of pore fluid pressure from an upstream fluid reservoir of fixed volume, across a permeable sample to atmosphere such that:

$$k_D = \frac{2L\mu}{A} \frac{V_u}{P_u^2 - P_d^2} \frac{dP_u}{dt}. \quad (3)$$

where V_u is the volume of the upstream pore fluid reservoir. If the downstream reservoir is infinite, the volume of the upstream reservoir can be measured experimentally and is given by the slope of Q as a function of $\frac{\partial P_u}{\partial t}$, multiplied by P_d:

$$V_u = \frac{P_d Q}{\partial P_u / \partial t}. \quad (4)$$

Permeability, k_D, is calculated using Eq. (3) when the relationship between $\frac{dP_u}{dt}$ and $P_u^2 - P_d^2$ is well described by a linear function; deviations from a linear relationship indicate the need to assess the data for Forchheimer and Klinkenberg effects.

Both methods described above give k_D for different values of ΔP, therefore the data can be assessed for fluid flow related artefacts including turbulent flow (i.e. the Forchheimer effect) and/or gas slip along flow channel walls (i.e. the Klinkenberg effect). The need for a Forchheimer correction is assessed first. This is done by plotting $1/k_D$ for each ΔP as a function of Q. The Forchheimer correction is necessary if the data are well described by a positive linear relationship. In this study, if the data are well described by Darcy's Law (Eqs. (2) or (3)) we consider a Forchheimer correction only if the linear relationship between $1/k_D$ and Q has an $R^2 > 0.99$. While this threshold R^2 is arbitrary, we apply it so as to minimize subjectivity in our data analysis. The Forchheimer-corrected permeability k_{forch} is then taken as the inverse of the y-intercept of the best-fit linear regression of this positive linear relationship.

To check for the Klinkenberg effect, a Forchheimer-corrected permeability, k_c, is calculated for each ΔP:

$$\frac{1}{k_c} = \frac{1}{k_D} - \xi Q \quad (5)$$

where ξ is the slope of the graph of $1/k_D$ as a function of Q. Subsequently, k_c is assessed as a function of $1/P_m$. The Klinkenberg correction is necessary if these data are well described by a positive linear relationship (again assessed as having an $R^2 > 0.99$), and the sample permeability is taken as the y-intercept of the best-fit linear regression of the data. If the data on the graph of k_c as a function of $1/P_m$ cannot be described by a positive linear relationship, then the permeability of the sample is k_{forch}. In the absence of a Forchheimer correction, the need for a Klinkenberg correction is determined by assessing k_D as a function of $1/P_m$. In this case, the sample permeability, k_{klink}, is the y-intercept of the best-fit linear regression of the plot of k_D as a function of $1/P_m$. If no corrections are deemed necessary, then the sample permeability is k_D.

3.2. Introducing a tensile fracture

To introduce a through-going tensile fracture in each of our samples, we followed a procedure similar to that outlined by Nara et al. (2011), Heap and Kennedy (2016), Hofmann et al. (2016); Wang et al. (2016), and Lamur et al. (2017), amongst others. Once the initial connected porosities and permeabilities of the samples were determined, each sample was wrapped in a single layer of electrical tape before being diametrically loaded in compression in a servo-controlled uniaxial press at a constant loading rate of 200 N/s until the formation

of a through-going tensile fracture parallel to the sample axis. The creation of a through-going tensile fracture was signaled by a mechanical drop in force; we confirmed the creation of the fracture visually and arrested the motor manually to prevent the formation of ancillary fractures. The majority of samples contained a single through-going fracture. In a limited number of samples, more than one through-going tensile fracture was created; these samples were discarded (noted in Table 1). We note that the diameter of our samples is much smaller than the recommended minimum requirement of the International Society of Rock Mechanics (core diameter > 54 mm) (Ulusay and Hudson, 2007); therefore, we have not determined the tensile strength of these materials. Following sample failure, the permeability of the fractured samples, k, was measured with the fracture plane oriented parallel to the fluid flow direction (Fig. 2B).

The cross-sectional areas A (the entire sample), A_i (the intact rock), and A_f (the fracture) were determined for each sample in 2D using the image-processing software ImageJ. Fracture tortuosity was calculated: $\tau = l_p/l_s$, where l_p is the fracture length and l_s is the shortest distance between fracture tips (Table 1, Fig. 2A). The average fracture width, d, was determined by dividing the fracture area, A_f, by the fracture length, l_p (Table 1). In some samples, secondary fractures developed during deformation (Fig. 2A); as these were not through-going fractures, we did not include them in our analysis of tortuosity nor did we include their cross-sectional areas in our calculations of fracture permeability.

4. Results

The range of permeability values of the intact sandstone, k_i, is between 4×10^{-19} to 1×10^{-14} m^2 (Table 1; Fig. 3). Permeability increases with increasing connected porosity (Table 1; black circles in Fig. 3), as previously demonstrated for the same rocks by Heap et al. (2017). The experimentally produced fractures are between 0.1 and 0.8 mm wide and the permeability of the fractured samples, k, is between 8×10^{-14} to 4×10^{-12} m^2 (Table 1; white circles in Fig. 3); the permeability of the fractured samples increases with average fracture width (Fig. 4A). We note that samples with the lowest initial porosity experienced an increase in permeability of nearly six orders of magnitude, while the permeability of initially high porosity samples increased by just over one order of magnitude (Fig. 3). Further, the introduction of through-going tensile fractures not only raised the permeability of the samples by as much as six orders of magnitude but also reduced the range of permeability to only two orders of magnitude.

The permeability of the introduced fractures is calculated by rearranging Eq. (1) such that: $k_f = \frac{Ak - A_i k_i}{A_f}$, where k_f and A_f are the permeability and cross sectional area of the fracture, respectively (Fig. 2A).

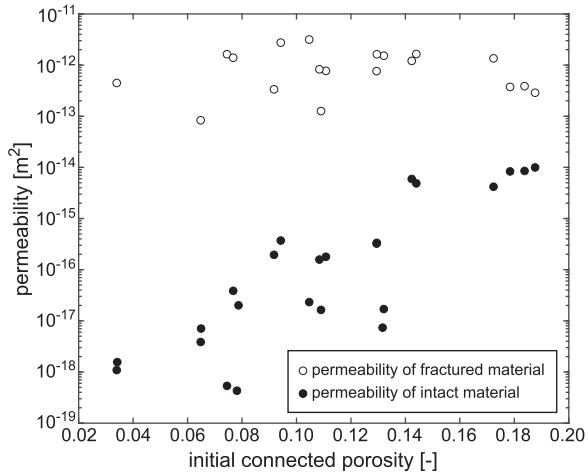

Fig. 3. Permeability of the intact and fractured samples as a function of initial connected porosity.

The permeability of the fractured samples was measured under a confining pressure of 1 MPa, thus the fracture apertures at the time of measurement were likely smaller than observed (Fig. 2A). However, we assume that the closure of these fractures is minimal due to the presence of asperities and loose grains at the fracture surfaces. Thus, for simplicity, we have assumed fracture areas and widths equal to the values of A_f and d determined by image analysis. Fracture permeability ranges between 1×10^{-11} to 3×10^{-10} m^2 (Table 1). The tortuosity of all fractures is between 1.02 and 1.10.

5. Discussion

5.1. Matrix and fracture permeability

Overall, the matrix permeability of the intact rocks decreases with decreasing connected porosity (Fig. 3) and is in accordance with previously reported laboratory measurements on rocks from the EPS-1 borehole (Griffiths et al., 2016; Heap et al., 2017). However, these sandstones are less permeable than other porous sandstones (Bourbié and Zinszner, 1985; David et al., 1994; Zhu and Wong, 1997; Vajdova et al., 2004; Baud et al., 2012; Wadsworth et al., 2016) owing to the occurrence of pore filling alteration to the permeable network including illite-smectite, siderite, barite, and carbonate precipitation (Griffiths et al., 2016; Heap et al., 2017). The introduction of fractures has a normalizing effect on the magnitude of the sample permeability (Fig. 3). While the permeability of the intact material spans five orders of magnitude between 4.23×10^{-19} to 9.80×10^{-15} m^2, the permeability of the fractured samples rises to between 8.20×10^{-14} and 3.10×10^{-12} m^2. Despite this large disparity in the magnitude of the change in permeability, the permeability values of the fractured samples collapse to within two orders of magnitude of each other. As previously observed, the relative increase in permeability is greatest for initially low-permeability samples (e.g. Heap and Kennedy (2016); Lamur et al. (2017); Pérez-Flores et al. (2017)). For example, while the permeability increased by just over one order of magnitude in the high-porosity ($\phi_c = 0.18$) *Rehberg* unit (samples 347_1 and 347_2, Table 1), permeability increased by over six orders of magnitude in the low-porosity ($0.03 < \phi_c < 0.08$) *Annweiler* unit (sample 508_1, Table 1).

The tortuosity of the fractures ranges between 1.02 and 1.10 (Table 1) and is not correlated with fracture permeability (Fig. 4B). This is in contrast to measurements on volcanic rocks (Heap and Kennedy, 2016), which exhibit a clear negative correlation between fracture permeability and tortuosity for the same range of fracture tortuosity observed in the present study. One possible reason for this is that the sandstones are more microstructurally homogenous than the andesites of Heap and Kennedy (2016), which contain vesicles and crystals that act to deflect propagating fractures, exacerbating fracture tortuosity. We note that the tortuosity values reported in both studies are calculated using the surface expression of the fracture on the sample end-face (Fig. 2B) and thus, only account for the fracture tortuosity expressed in 2D on that surface and orthogonal to fluid flow; fracture tortuosity along the length of the sample is not accounted for.

5.2. Scaling permeability to the reservoir

The values of permeability described above cannot be immediately applied to the reservoir scale. The equivalent permeability of a rock unit containing a single planar feature perpendicular (Freeze and Cherry, 1979; Vajdova et al., 2004) or parallel (Farquharson et al., 2016b; Heap and Kennedy, 2016) to fluid flow has been previously presented. When several fractures are oriented parallel to fluid flow, the equivalent permeability of the rock unit can be described by:

$$k_e = \frac{w_i k_i + \sum_{j=1}^{N} w_{fj} k_{fj}}{W} \quad (6)$$

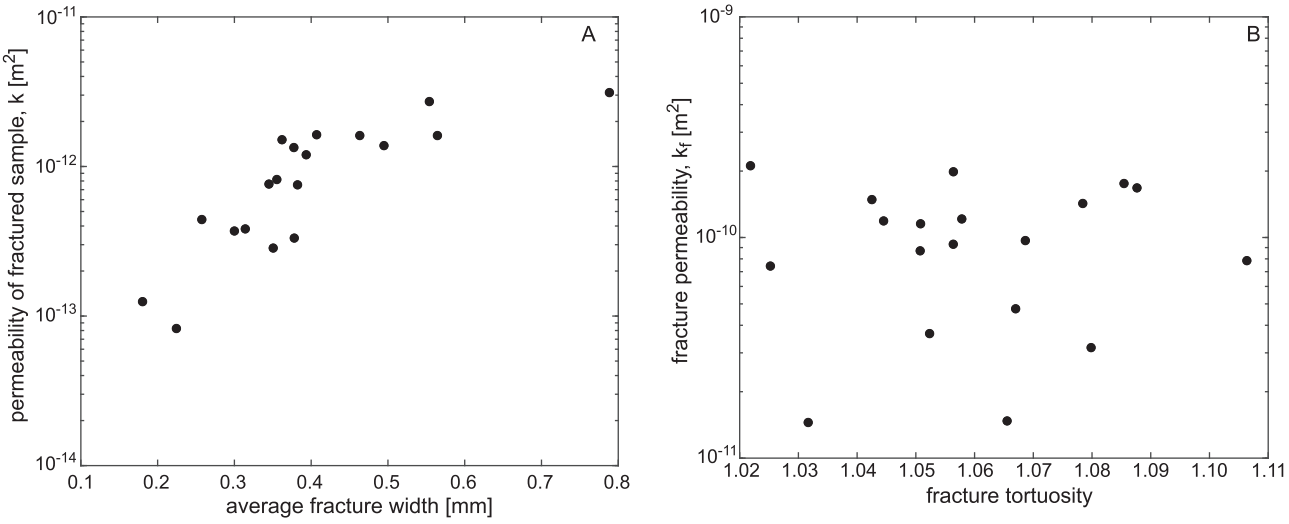

Fig. 4. A. Permeability of the fractured samples as a function of average fracture width. B. Fracture permeability as a function of fracture tortuosity.

where k_e is the equivalent permeability of a rock unit containing N fractures of width w_f and permeability k_f, w_i is the width of intact rock, and W is the total width of the rock unit in question (Farquharson et al., 2017b).

To determine the equivalent permeability along the depth of the EPS-1 borehole, we use the fracture apertures with depth reported from borehole televiewer logs (Vernoux et al., 1995; Genter and Traineau, 1996; Genter et al., 1997). These data provide fracture populations with depth for 1) all existing fractures, including open and filled fractures and 2) open fractures only. EPS-1 can be divided into seven discreet fracture zones and the total average fracture aperture per zone roughly decreases with depth from 1.9 mm in the uppermost zone (1008–1020 m; the *Voltzia* unit) to 0.8 mm in the lowermost zone (1381–1416 m; the *Annweiler* and *Anté-Annweiler* units) (Haffen et al., 2013). Using Eq. (6), we take w_f to be the sum of the apertures of all fractures for each interval W down EPS-1; in this study we determine equivalent permeability over intervals of $W = 20$ m. k_f and k_i are the average measured fracture and intact rock permeability values for each interval, respectively.

We note that the Mode I fractures induced in this study were not created under in situ conditions, that is, under conditions pertinent to a sample's depth in the borehole. The fractures observed at depth by borehole televiewer likely remained open because of small amounts of shear that resulted in the misalignment of their surfaces (e.g. Hofmann et al. (2016) and Pérez-Flores et al. (2017)). Indeed, fracture surface misalignment results in an increase in fracture permeability of several orders of magnitude with respect to perfectly mated fracture surfaces (Pérez-Flores et al., 2017). We do not contend that the fractures created in this study reflect the processes operative at depth. Instead, we have chosen to introduce Mode I fractures experimentally so as to be able to quantify the permeability of fractures of known widths oriented parallel to fluid flow. Further, we note that the permeability measurements performed in this study were not made under in situ conditions. While it is clear that fracture permeability decreases as fracture aperture is closed in response to increasing effective pressure (Kranz et al., 1979; Pyrak-Nolte et al., 1987; Nara et al., 2011; Hofmann et al., 2016; Lamur et al., 2017; Nara et al., 2017; Pérez-Flores et al., 2017; Watanabe et al., 2017), we assume that the values of fracture permeability determined in this study reflect the permeability of fractures of fixed width d for a given lithology and that these values are applicable to fractures of fixed width d at depth.

Assuming that all the fractures (open and filled) in EPS-1 are opened, the presence of the fractures raises the equivalent permeability of all rock units to between 7×10^{-15} and 2×10^{-12} m^2 (Fig. 5, white circles), with particularly high equivalent permeability zones located in the *Rehberg* unit. High equivalent permeability zones associated with the *Rehberg* unit are correlated with the presence of the Soultz fault (Vernoux et al., 1995). Despite the low connected porosity of the matrix rock, the large change in equivalent permeability of the *Annweiler* unit is associated with high fracture density (2 fractures/m, Haffen et al. (2013)). All equivalent permeability values calculated herein, with the exception of the equivalent permeability at the *Karlstal-Rehberg* interface, are greater than the proposed minimum system permeability of 10^{-14} m^2 needed to sustain hydrothermal fluid convection within the reservoir at Soultz-sous-Forêts (Graf and Therrien, 2009; Magnenet et al., 2014).

We emphasize that we have assumed that the fracture width, w_f, is the sum of the apertures of all the fractures for an interval length of 20 m (Farquharson et al., 2017b). While arithmetically identical to the case of N fractures of width w_f/N, fluid flow through one large fracture is likely not equivalent to fluid flow through several small fractures. Large fractures can potentially exacerbate non-laminar fluid flow conditions, while small fracture apertures may incur a Klinkenberg effect in systems where the pore fluid is gaseous. Further, upscaling fracture sizes may not account for heterogeneities on a variety of scales that affect fracture tortuosity. Finally, in this study the permeant is an inert gas, which precludes the chemical interactions that may occur naturally in the reservoir in the presence of a briny geothermal fluid or the interaction of clay with water (Faulkner and Rutter, 2000; Tanikawa and Shimamoto, 2006; Davy et al., 2007; Tanikawa and Shimamoto, 2009) and, thus, the permeability values reported herein represent maximum permeability values.

5.3. Implications for the exploitation of geothermal resources

Stober and Bucher (2015) compiled hydraulic conductivity data for the Buntsandstein from borehole tests performed at 14 sites throughout the Upper Rhine Graben. Generally, the hydraulic conductivity of the Buntsandstein decreases with increasing depth, ranging between 1×10^{-11} and 1×10^{-5} m.s^{-1} down to a depth of 3000 m below the surface (Stober and Bucher, 2015). Hydraulic conductivity can be converted to permeability: $k = \frac{K\mu}{g\rho}$, where K is the hydraulic conductivity (m.s^{-1}), μ and ρ are the dynamic viscosity (Pa.s) and density (kg.m^{-3}) of the fluid, respectively – here we assume the dynamic viscosity (2.16×10^{-7} Pa.s) and density (941.3 kg.m^{-3}) of water at 130 °C and 13 MPa, consistent with the in situ pore fluid pressure (Cornet et al., 2007) – and g is the acceleration due to gravity at the surface (9.8 m.s^{-2}). The median permeability for the Buntsandstein

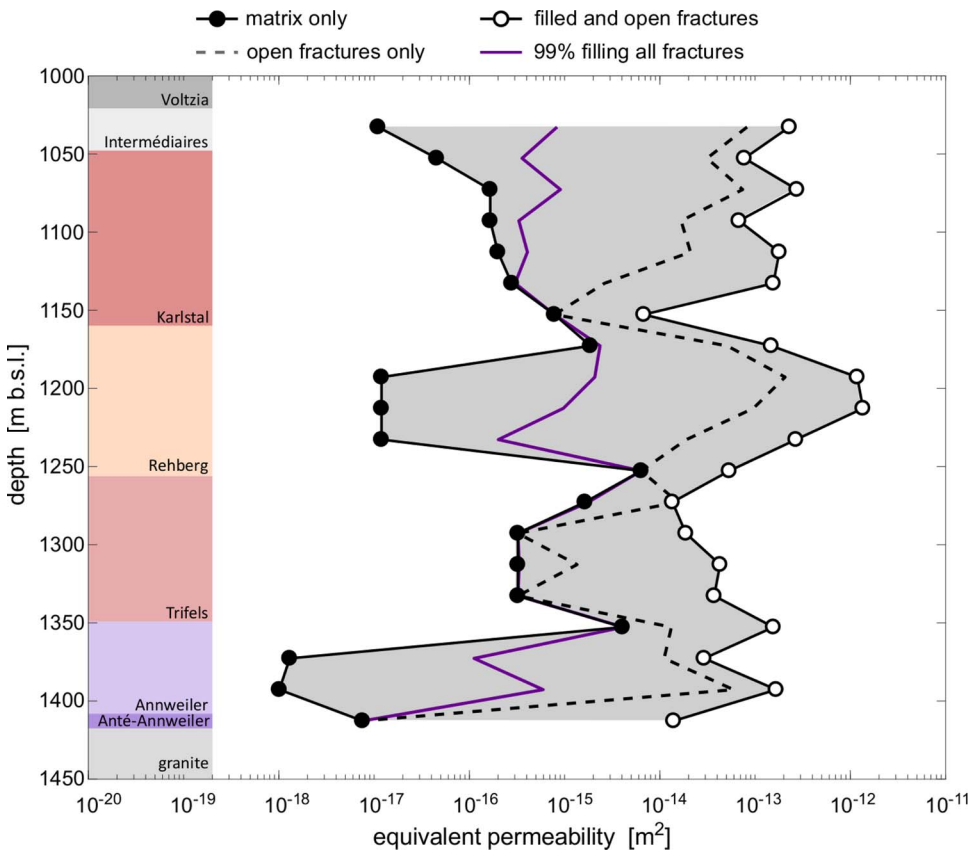

Fig. 5. The equivalent permeability of the Permo-Triassic sediments down the EPS-1 borehole, calculated over 20 m intervals down the borehole. Black circles: equivalent permeability calculated assuming no open fracture space (i.e. matrix only); White circles: equivalent permeability calculated assuming that all observed fractures are open. The dashed black line denotes the equivalent permeability determined using the open fracture space, as observed using borehole televiewer data (Genter and Traineau, 1996). The purple line assumes that only 1% of the total fracture space is open. Note: The intact and fractured sample permeability values used to calculate equivalent permeability were measured under a confining pressure of 1 MPa and ambient laboratory temperature.

calculated from the hydraulic conductivity data is 5.7×10^{-15} m^2 (the 1st and 3rd quartiles are 8.8×10^{-16} m^2 and 5.1×10^{-14} m^2, respectively) (Stober and Bucher, 2015). The permeability of the intact sandstone measured in this study is between 4×10^{-19} m^2 and 1×10^{-14} m^2 (Fig. 5; black circles), which is notably lower than the permeability of the Buntsandstein determined from field hydraulic conductivity tests. Further, we note that the equivalent permeability, k_e, of the Buntsandstein when all observed fractures are assumed to be open (7×10^{-15} m^2 and 2×10^{-12} m^2; Fig. 5, white circles) is greater than that predicted by hydraulic borehole tests.

The model presented above (see Section 5.2) assumes that the fracture space is completely open, which is not necessarily consistent with the observation of extensive secondary mineral precipitation within the Buntsandstein (Nollet et al., 2009; Griffiths et al., 2016). Borehole televiewer records of exploratory and production wells at Soultz-sous-Forêts confirm the presence of large-scale fracture zones throughout the sedimentary cover, which are variably sealed by secondary mineral precipitation (Genter et al., 1997). When we consider only fractures observed by borehole televiewer to be open, the predicted equivalent permeability down the borehole (7×10^{-18} m^2 and 3×10^{-13} m^2; Fig. 5, dotted line) is consistent with the data compiled by Stober and Bucher (2015). Further, modelling the equivalent permeability with depth when 99% of the total fracture space is sealed, we find that the system has a permeability range between 7×10^{-18} to 7×10^{-15} m^2 (Fig. 5, purple line). Thus, while the range of permeability calculated assuming that all observed fractures are open is above the threshold permeability needed to sustain geothermal convection cells within the Soultz-sous-Forêts geothermal reservoir (Graf and Therrien, 2009; Magnenet et al., 2014), fracture sealing due to mineral precipitation will progressively impede hydrothermal circulation. As an example, assuming a fluid temperature of ≈ 130 °C (consistent with the resident Buntsandstein temperature) and a radial growth rate of 1.5×10^{-2} mm/day, uninhibited barite precipitation could entirely seal fractures 2 mm wide (the mean fracture width in EPS-1) within one month (Griffiths et al., 2016), reducing the equivalent permeability to less than 10^{-14} m^2. We emphasize that this simple model accounts for neither channelized flow (Méheust and Schmittbuhl, 2001) nor changes in brine composition, which may result in spatially variable precipitation rates. Thus, this simple calculation represents the shortest time needed to achieve fracture sealing. Indeed, open and partially sealed fractures are observed in the Buntsandstein (Genter et al., 1997), suggesting that processes acting to keep fractures open (e.g. slip along fractures) are operative. Nevertheless, partial fracture-sealing will act to reduce the equivalent permeability of the sedimentary cover to below 10^{-14} m^2, retarding large-scale hydrothermal convection and necessitating anthropogenic stimulation of the reservoir to maintain economically viable geothermal energy production.

6. Conclusions

Quantifying the role of large-scale fractures on the equivalent permeability of geothermal reservoirs in the laboratory is currently hampered by sample scale, generally restricting such measurements to intact rock and thus underestimating the permeability of the reservoir by several orders of magnitude. Here we present a simple procedure with which the permeability of fluid reservoirs in the crust can be assessed for economic purposes. By measuring the permeability of initially intact sandstone procured from the EPS-1 borehole before and after the introduction of a through-going tensile fracture, we demonstrate that fractures increase sample permeability by up to six orders of magnitude. Further, the presence of a fracture is sufficient to limit the range of permeability of all samples to within two orders of magnitude. These values are used to inform modelling of the equivalent permeability of the sandstone units at the metre-scale. The range of calculated equivalent permeability values when all open fracture space down the EPS-1 borehole is considered (between 7×10^{-18} and 3×10^{-13} m^2) are in agreement with the range of hydraulic conductivities measured at the borehole scale but are not sufficiently high to support sustained

hydrothermal convection in the geothermal reservoir at Soultz-sous-Forêts. This simple workflow can aid in the assessment of the economic viability of not only geothermal reservoirs, but any fluid reservoir of economic interest, including petroleum and natural gas.

Conflict of interest

The authors declare no competing interests.

Acknowledgements

ARLK acknowledges funding provided by the Agence Nationale de la Recherche (ANR) grant CANTARE (ANR-15-CE06-0014-01). The authors also acknowledge LABEX grant ANR-11-LABX-0050_G-EAU-THERMIE-PROFONDE; this research benefited from state funding managed by the ANR as part of the "Investissements d'avenir" program. We thank Albert Genter, Chrystal Dezayes, Bertrand Renaudié, Coralie Aichholzer, Philippe Duringer, Jamie Farquharson, and Luke Griffiths. We thank two anonymous reviewers for their constructive comments, which helped to clarify the manuscript.

References

Aichholzer, C., Duringer, P., Orciani, S., Genter, A., 2016. New stratigraphic interpretation of the Soultz-sous-Forêts 30-year-old geothermal wells calibrated on the recent one from Rittershoffen (Upper Rhine Graben, France). Geotherm. Energy 4 (13).

Baria, R., Baumgärtner, J., Gérard, A., Jung, R., Garnish, J., 1999. European HDR research programme at Soultz-sous-Forêts (France) 1987–1996. Geothermics 28 (4–5), 655–669.

Baud, P., Meredith, P., Townend, E., 2012. Permeability evolution during triaxial compaction of an anisotropic porous sandstone. J. Geophys. Res.-Solid Earth 117.

Baujard, C., Genter, A., Dalmais, E., Maurer, V., Hehn, R., Rosillette, R., Vidal, J., Schmittbuhl, J., 2017. Hydrothermal characterization of wells GRT-1 and GRT-2 in Rittershoffen, France: implications on the understanding of natural flow systems in the Rhine graben. Geothermics 65, 255–268.

Baumgärtner, J., Lerch, C., 2013. Geothermal 2.0: the insheim geothermal power plant. the second generation of geothermal power plants in the upper rhine graben. Paper Presented at Proceedings of Third European Geothermal Review.

Bourbié, T., Zinszner, B., 1985. Hydraulic and acoustic properties as a function of porosity in Fontainbleau sandstone. J. Geophys. Res. 90 (B13), 1524–1532.

Brace, W.F., Walsh, J.B., Frangos, W.T., 1968. Permeability of granite under high pressure. J. Geophys. Res. 73, 2225–2236.

Brace, W.F., 1978. A note on permeability changes in geologic material due to stress. Pure Appl. Geophys. 116 (4–5), 627–633.

Brown, S.R., 1987. Fluid-flow through rock joints – the effect of surface-roughness. J. Geophys. Res.-Solid Earth Planets 92 (B2), 1337–1347.

Brown, S.R., 1989. Transport of fluid and electric current through a single fracture. J. Geophys. Res. 94 (B7), 9429–9438.

Caine, J.S., Evans, J.P., Forster, C.B., 1996. Fault zone architecture and permeability structure. Geology 24 (11), 1025–1028.

Christy, A.G., Putnis, A., 1993. The kinetics of barite dissolution and precipitation in water and sodium-chloride brines at 44–85 °C. Geochim. Cosmochim. Acta 57 (10), 2161–2168.

Cornet, F.H., Berard, T., Bourouis, S., 2007. How close to failure is a ganite rock mass at a 5 km depth? Int. J. Rock Mech. Min. Sci. 44 (1), 47–66.

David, C., Wong, T.F., Zhu, W.L., Zhang, J.X., 1994. Laboratory measurements of compaction-induced permeability change in porous rocks – implications for the generation and maintenance of pore pressure excess in the crust. Pure Appl. Geophys. 143 (1–3), 425–456.

Davy, C.A., Skoczylas, F., Barnichon, J.-D., Lebon, P., 2007. Permeability of macro-cracked argillite under confinement: gas and water testing. Phys. Chem. Earth Parts A/B/C/ 32 (8–14), 667–680.

Dezayes, C., Genter, A., Valley, B., 2010. Structure of the low permeable naturally fractured geothermal reservoir at Soultz. C. R. Geosci. 342 (7–8), 517–530.

Farquharson, J.I., Heap, M.J., Baud, P., 2016a. Strain-induced permeability increase in volcanic rock. Geophys. Res. Lett. 43 (22), 11603–11610.

Farquharson, J.I., Heap, M.J., Lavallee, Y., Varley, N.R., Baud, P., 2016b. Evidence for the development of permeability anisotropy in lava domes and volcanic conduits. J. Volcanol. Geotherm. Res. 323, 163–185.

Farquharson, J., Baud, P., Heap, M.J., 2017a. Inelastic compaction and permeability evolution in volcanic rock. Solid Earth 8, 561–581.

Farquharson, J., Wadsworth, F.B., Heap, M.J., Baud, P., 2017b. Time-dependent permeability evolution in compacting volcanic fracture systems and implications for gas overpressure. J. Volcanol. Geotherm. Res. 339, 81–97.

Faulkner, D.R., Rutter, E., 2000. Comparisons of water and argon permeability in natural clay-bearing fault gouge under high pressure at 20 °C. J. Geophys. Res. 105 (B7), 415–416.

Forchheimer, P., 1901. Water movement through ground. Zeitschrift Des Vereines Deutscher Ingenieure 45, 1736–1741.

Freeze, R.A., Cherry, J.A., 1979. Groundwater. Prentice-Hall.

Gérard, A., Genter, A., Kohl, T., Lutz, P., Rose, P., Rummel, F., 2006. The deep EGS (Enhanced geothermal system) project at Soultz-sous-Forêts (Alsace, France). Geothermics 35 (5–6), 473–483.

Genter, A., Traineau, H., 1996. Analysis of macroscopic fractures in granite in the HDR geothermal well EPS-1, Soultz-sous-Forets, France. J. Volcanol. Geotherm. Res. 72 (1–2), 121–141.

Genter, A., Castaing, C., Dezayes, C., Tenzer, H., Traineau, H., Villemin, T., 1997. Comparative analysis of direct (core) and indirect (borehole imaging tools) collection of fracture data in the Hot Dry Rock Soultz reservoir (France). J. Geophys. Res.-Solid Earth 102 (B7), 15419–15431.

Graf, T., Therrien, R., 2009. Stable-unstable flow of geothermal fluids in fractured rock. Geofluids 9, 138–152.

Griffiths, L., Heap, M.J., Wang, F., Daval, D., Gilg, H.A., Baud, P., Schmittbuhl, J., Genter, A., 2016. Geothermal implications for fracture-filling hydrothermal precipitation. Geothermics 64, 235–245.

Guillou-Frottier, L., Carre, C., Bourgine, B., Bouchot, V., Genter, A., 2013. Structure of hydrothermal convection in the Upper Rhine Graben as inferred from corrected temperature data and basin-scale numerical models. J. Volcanol. Geotherm. Res. 256, 29–49.

Haffen, S., Geraud, Y., Diraison, M., Dezayes, C., 2013. Determination of fluid-flow zones in a geothermal sandstone reservoir using thermal conductivity and temperature logs. Geothermics 46, 32–41.

Heap, M.J., Kennedy, B.M., 2016. Exploring the scale-dependent permeability of fractured andesite. Earth Planet. Sci. Lett. 447, 139–150.

Heap, M.J., Kushnir, A.R.L., Gilg, H.A., Wadsworth, F.B., Reuschlé, T., Baud, P., 2017. Microstructural and petrophysical properties of the Permo-Triassic sandstones (Buntsandstein) from the Soultz-sous-Forêts geothermal site (France). Geotherm. Energy 5 (26).

Hettkamp, T., Baumgärtner, J., Teza, D., Lerch, C., 2013. Experiences from 5 years operation in Landau. Paper Presented at Proceedings of Third European Geothermal Review.

Hofmann, H., Bloecher, G., Milsch, H., Babadagli, T., Zimmermann, G., 2016. Transmissivity of aligned and displaced tensile fractures in granitic rocks during cyclic loading. Int. J. Rock Mech. Min. Sci. 87, 69–84.

Housse, B.A., 1984. Reconnaissance du potentiel géothermique du Buntsandstein à Strasbourg-CronenbourgRep.

Kappelmeyer, O., Gérard, A., Schloemer, W., Ferrandes, R., Rummel, F., Benderitter, Y., 1991. European HDR project at Soultz-sous-Forêts: general presentation. Geotherm. Sci. Technol. 2 (4), 263–289.

Klinkenberg, L.J., 1941. The permeability of porous media to liquids and gases. Drill. Prod. Pract. 200–213.

Kranz, R.L., Frankel, A.D., Engelder, T., Scholz, C.H., 1979. The permeability of whole and jointed Barre granite. Int. J. Rock Mech. Min. Sci. Geomech. Abstr. 16 (4), 225–234.

Lamur, A., Kendrick, J.E., Eggertsson, G.H., Wall, R.J., Ashworth, J.D., Lavallée, Y., 2017. The permeability of fractured rocks in pressurised volcanic and geothermal systems. Sci. Rep. 7, 1–9.

Ledesert, B., Hebert, R., Genter, A., Bartier, D., Clauer, N., Grall, C., 2010. Fractures, hydrothermal alterations and permeability in the Soultz enhanced geothermal system. C. R. Geosci. 342 (7–8), 607–615.

Lundgren, P., Casu, F., Manzo, M., Pepe, A., Berardino, P., Sansosti, E., Lanari, R., 2004. Gravity and magma induced spreading of Mount Etna volcano revealed by satellite radar interferometry. Geophys. Res. Lett. 31, L04602. http://dx.doi.org/10.1029/2003GL018736.

Méheust, Y., Schmittbuhl, J., 2001. Geometrical heterogeneities and permeability anisotropy of rough fractures. J. Geophys. Res. 106 (B2), 2089–2102.

Magnenet, V., Fond, C., Genter, A., Schmittbuhl, J., 2014. Two-dimensional THM modelling of the large scale natural hydrothermal circulation at Soultz-sous-Forêts. Geotherm. Energy 2 (17).

Min, K.B., Rutqvist, J., Tsang, C.F., Jing, L.R., 2004. Stress-dependent permeability of fractured rock masses: a numerical study. Int. J. Rock Mech. Min. Sci. 41 (7), 1191–1210.

Mitchell, T.M., Faulkner, D.R., 2008. Experimental measurements of permeability evolution during triaxial compression of initially intact crystalline rocks and implications for fluid flow in fault zones. J. Geophys. Res. 113 (B11412).

Moore, D.E., Lockner, D.A., Byerlee, J.D., 1994. Reduction of permeability in granite at elevated-temperatures. Science 265 (5178), 1558–1561.

Morrow, C.A., Moore, D.E., Lockner, D.A., 2001. Permeability reduction in granite under hydrothermal conditions. J. Geophys. Res.-Solid Earth 106 (B12), 30551–30560.

Nara, Y., Meredith, P.G., Yoneda, T., Kaneko, K., 2011. Influence of macro-fractures and micro-fractures on permeability and elastic wave velocities in basalt at elevated pressure. Tectonophysics 503 (1–2), 52–59.

Nara, Y., Kato, M., Niri, R., Kohno, M., Sato, T., Fukuda, D., Sato, T., Takahashi, M., 2017. Permeability of granite including macro-fracture naturally filled with fine-grained minerals. Pure Appl. Geophys. 1–11.

Nollet, S., Koerner, T., Kramm, U., Hilgers, C., 2009. Precipitation of fracture fillings and cements in the Buntsandstein (NW Germany). Geofluids 9 (4), 373–385.

Pérez-Flores, P., Wang, G., Mitchell, T.M., Meredith, P.G., Nara, Y., Sarkar, V., Cembrano, J., 2017. The effect of offset on fracture permeability of rocks from the Southern Andes Volcanic Zone, Chile. J. Struct. Geol. 104, 142–158.

Pribnow, D., Schellschmidt, R., 2000. Thermal tracking of upper crustal fluid flow in the Rhine Graben. Geophys. Res. Lett. 27 (13), 1957–1960.

Pyrak-Nolte, L.J., Myer, L.R., Cook, N.G.W., Witherspoon, P.A., 1987. Hydraulic and mechanical properties of natural fractures in low permeabillity rock. In: Herget, G., Vongpaisal, S. (Eds.), Proceedings of the 6th International Congress of Rock

Mechanics. Balkema Rotterdam. pp. 225–231.
Sausse, J., Fourar, M., Genter, A., 2006. Permeability and alteration within the Soultz granite inferred from geophysical and flow log analysis. Geothermics 35 (5–6), 544–560.
Scheiber, J., Seibt, A., Birner, J., Genter, A., Moeckes, W., 2013. Application of a scaling inhibitor system at the geothermal power plant in Soultz-sous-Forêts: laboratory and on-site studies. Paper Presented at Proceedings European Geothermal Congress.
Stober, I., Bucher, K., 2015. Hydraulic and hydrochemical properties of deep sedimentary reservoirs of the Upper Rhine Graben, Europe. Geofluids 15, 464–482.
Summers, R., Winkler, K.W., Byerlee, J., 1978. Permeability changes during the flow of water through westerly granite at temperatures of 100–400 °C. J. Geophys. Res. 183 (B1), 339–344.
Tanikawa, W., Shimamoto, T., 2006. Klinkenberg effect for gas permeability and its comparison to water permeability for porous sedimentary rocks. Hydrol. Earth Syst. Sci. Discuss. 3 (4), 1315–1338.
Tanikawa, W., Shimamoto, T., 2009. Comparison of Klinkenberg-corrected gas permeability and water permeability in sedimentary rocks. Int. J. Rock Mech. Min. Sci. 46, 229–238.
Thompson, M.E., Brown, S.R., 1991. The effect of anisotropic surface-roughness on flow and transport in fractures. J. Geophys. Res. 96 (B13), 21923–21932.
Tsang, Y.W., 1984. The effect of tortuosity on fluid flow through a single fracture. Water Resour. Res. 20 (9), 1209–1215.
Ulusay, R., Hudson, J.A., 2007. SM for determining tensile strength of rock materials – 1978 [EUR 4], part 2 – SM for determining indirect tensile strength by the Brazil test. In: Ulusay, R., Hudson, J.A. (Eds.), The Complete ISRM Suggested Methods for Rock Characterization, Testing and Monitoring: 1974–2006, (ISBN 978-975-93675-4-1).
Vajdova, V., Baud, P., Wong, T.F., 2004. Permeability evolution during localized deformation in Bentheim sandstone. J. Geophys. Res. 109 (B10406).
Vernoux, J.F., Genter, A., Razin, P., Vinchon, C., 1995. Geological and Petrophysical Parameters of a Deep Fractured Sandstone Formation as Applied to Geothermal Exploitation. EPS-1 borehole, Soults-sous-Forêts, FranceRep., BRGM France.
Vidal, J., Genter, A., Schmittbuhl, J., 2015. How do permeable fractures in the Triassic sediments of northern Alsace characterize the top of hydrothermal convective cells? Evidence from Soultz geothermal boreholes (France). Geotherm. Energy 3 (8).
Villadangos, G., 2013. ECOGI, EGS Upper Rhine Geothermal project for the industry, first well and result. Proceedings of Third European Geothermal Review.
Wadsworth, F.B., Vasseur, J., Scheu, B., Kendrick, J.E., Lavallée, Y., Dingwell, D., 2016. Universal scaling of fluid permeability during volcanic welding and sediment diagenesis. Geology 44 (3), 219–222.
Walsh, J.B., 1981. Effect of pore pressure and confining pressure on fracture permeability. Int. J. Rock Mech. Min. Sci. 18 (5), 429–435.
Wang, G., Mitchell, T.M., Meredith, P.G., Nara, Y., Wu, Z., 2016. Influence of gouge thickness and grain size on permeability of macrofractured basalt. J. Geophys. Res. Solid Earth 121 (12), 8472–8487.
Watanabe, N., Numakura, T., Sakaguchi, K., Saishu, H., Okamoto, A., Ingebritsen, S.E., Tsuchiya, N., 2017. Potentially exploitable supercritical geothermal resources in the ductile crust. Nat. Geosci. 10 (2), 140-.
Witherspoon, P.A., Wang, J.S.Y., Iwai, K., Gale, J.E., 1980. Validity of cubic law for fluid flow in a deformable rock fracture. Water Resour. Res. 16 (6), 1016–1024.
Zhu, W., Wong, T.-F., 1997. The transition from brittle faulting to cataclastic flow: permeability evolution. J. Geophys. Res. 102 (B2), 3027–3041.
Zimmerman, R.W., Bodvarsson, G.S., 1996. Hydraulic conductivity of rock fractures. Transp. Porous Media 23, 1–30.
Zimmerman, R.W., Chen, D.W., Cook, N.G.W., 1992. The effect of contact area on the permeability of fractures. J. Hydrol. 139 (1–4), 79–96.